Leading edge stabilisation of vertical boundary layer diffusion flames

Vinny Gupta [a],[*], Tony Xiao [a], Matthew J. Dunn [a], José L. Torero [b], Assaad R. Masri [a]

[a] *University of Sydney, J07 Mechanical Engineering Building, Sydney, Australia*
[b] *University College London, Chadwick Building, London, UK*

A B S T R A C T

The leading edge stability of vertical boundary layer diffusion flames established over a 3D-printed porous gas burner is revealed through Planar Laser-Induced Fluorescence imaging of the OH radical (OH-PLIF). Flame stability is studied by premixing methane and ethylene with increasing volume fractions of bromotrifluoromethane (CF_3Br/Halon-1301) to increase the characteristic chemical timescale. Blow-off occurs at 15.7% and 37.3% CF_3Br addition for methane and ethylene respectively, which are remarkably large limits compared to other flame configurations. As CF_3Br is added, the flame stand-off distance increases and the reaction zone broadens, thereby increasing the flame length. This accelerates the buoyancy-induced flow ahead of the leading edge, promoting O_2 entrainment into the flame anchor. Consequently, the radical scavenging effects on the flame anchor reactivity are dampened, resulting in the flame re-anchoring slightly downstream along the plate. Towards extinction, the flame shortens dramatically due to efficient catalytic cycling and radiative quenching at the flame tip resulting from the brominated species and excessive soot formation. This reduces the O_2 mass flux into the kinetically dampened flame anchor resulting in blow-off extinction. Therefore, blow-off is controlled by both the leading edge reactivity and trailing edge length. Methane is shown to be considerably more sensitive compared to ethylene to CF_3Br owing to its larger flame speed. These results demonstrate that fire-induced buoyancy greatly increases blow-off limits when using chemically active or inert agents in vertical wall fire configurations.

1. Introduction

Boundary layer diffusion flames established over a fuel plate are highly relevant to understanding the phenomena of both opposed and concurrent flame spread [1]. Under both conditions, fuel is injected and then burned in a parallel oxidising flow, which may be provided by either forced convection over a horizontal plate through blowing or by natural convection over a vertical plate that is controlled by a buoyancy-induced flow. For stable flame cases far from blow-off, the infinitely fast chemistry assumption can be employed, leading to classical solutions for the boundary layer flame geometry for the burning of condensed fuels in both configurations in terms of the Spalding mass transfer number [2,3]. Assuming infinitely fast kinetics is not valid when approaching the blow-off branch; therefore, the classical boundary layer solutions do not hold. The blow-off limit for forced convection in a horizontal configuration has been extensively studied in both normal and microgravity environments by controlling the oxidiser co-flow velocity [4–6]. The work exploring blow-off in the horizontal

configuration has demonstrated that the boundary layer flame is anchored at the leading edge of the flame. Therefore, the structure and position of the anchor point are sensitive to the local Damköhler number at the leading edge [7]. It is well established that the anchor point structure is lifted above the fuel surface by a stand-off distance, and its structure is defined by a partially premixed edge flame structure [8], with stabilisation controlled by the local thermo-chemical and flow conditions.

Blow-off and flame stabilisation has not been well explored for vertical buoyancy-driven wall fires, which are canonically defined as boundary layer flames under natural convection. Most extinction studies for these types of flames focus on quenching at the trailing edge [9]. This is because the oxidiser velocity under natural convection is a dependent variable that is governed by the flame length and temperature. Thus, the local strain rate at the anchor point that defines the Damköhler number self-balances with the laminar boundary layer solution until the flame length becomes sufficiently long enough where flow separation occurs, and the flame becomes fully turbulent [10]. Despite this self-balancing

mechanism, it is still possible to induce strain-induced blow-off for vertically spreading condensed fuels that are sufficiently thin [11]. One aspect not studied in the literature for this configuration is the reduction in the Damköhler number by slowing the reaction rate either through chemical inhibition or by dilution [12,13]. This is the extinction sequence followed by many chemically active and inert fire retardants, however, no characterisation for the blow-off mechanism by chemical means exists.

This paper provides a detailed experimental insight into the progression towards blow-off for vertical buoyancy-driven boundary layer diffusion flames. The progression towards blow-off is achieved by reducing the Damköhler number at the leading edge of the flame by mixing increasing fractions of CF_3Br (Halon-1301) into CH_4 (methane) and C_2H_4 (ethylene) diffusion flames through the fuel-stream. CF_3Br is a well-known and highly effective inhibiting compound that relies on scavenging free radicals from chain branching reactions to increase the reaction rate [14]. This inhibiting compound was selected owing to its strong inhibition chemistry, which enable the reduction of the chemical timescale without significantly reducing the fuel mass fraction. CH_4 and C_2H_4 feature distinctly different laminar flame speeds and radical pool concentrations and therefore are expected to respond differently to CF_3Br addition. Comparing both fuels will be used to provide insight into the blow-off mechanism and the chemical interaction with the inhibitor. Planar laser-induced fluorescence (PLIF) imaging of the OH radical is undertaken at the leading edge of the flames for varying CF_3Br volume fractions. The effects of increasing the chemical timescale by CF_3Br addition on the flame structure, leading edge stability and flame chemistry is investigated.

2. Methodology

2.1. Experimental set-up

A novel 3D-printed porous stainless steel (17-4 PH) burner has been developed for this paper. The burner design is shown in Fig. 1, with a porous area of 50 × 50 mm, and a thickness of 25 mm. The burner pores were produced using a layered mesh structure, with a repeated unit cell profile per layer that created a sufficiently large enough pressure drop to establish uniform flow over the burner face to allow injection velocities similar to diffusion processes to be utilised. An additional motivation for the small unit cell size and low porosity is to enhance the thermal conductivity, hence a uniform preheat of the fuel stream over the burner face and an effective control of the overall burner temperature by the cooling water. Each of the unit cells is dimensioned at 0.75 × 0.75 mm. The cell structure and dimension define the porosity of the mesh, which

will be characterised in a future study. An ellipsoid-shaped (6 × 1.5 mm) water-cooling channel with 2 mm thick walls was printed 12.5 mm in-depth within the porous mesh. Both the water cooling and controlled mesh sizing are unique advantages of additive manufacturing that are often extraordinarily challenging to control using conventional hot-press sintering techniques that form traditional sintered bronze burners [15,16]. The burner was printed using a GE Concept Laser MLab 200R, with an overall build volume of 90 × 90 × 90 mm. Three burners were manufactured simultaneously during a single print session. The layer thickness of the 17-4H powder was 3 μm, and a d_{10} powder size of 17 μm. Upon testing the burner in a "flat flame" configuration with premixed methane-air at a range of equivalence ratios and flame speeds, it was discovered that due to the relatively small unit cell size that resulted in the melting of numerous cells across the layers the flow through the burner was not uniform in some areas. Considering that previous attempts with a units cell size of 600 μm resulted in a completely fused, solid matrix, we conclude that future designs using the same machine, powder and unit cell structure should be close to 1000 μm to avoid periodic fusing of the unit cell structure, the results of which will be reported in a future study. Despite the identified inhomogeneity observed in the flat flame configuration, for the present 750 μm unit cell burner, when operated in the vertical boundary layer configuration the flame anchor location and structure were found independent of burner orientation. This prototype demonstrates the advantages of additive manufacturing for burners whilst providing information on how further improvements could be made.

A bespoke gas plenum of 100 × 100 × 150 mm with two opposing gas inlet ports at the bottom of the chamber was manufactured to hold the burner and provide sealing in such a way that burners could be easily replaced. The burner is attached to an upper flange on the plenum and then mounted into a vertical steel plate such that the face of the porous mesh is flush against the vertical steel plate. Water cooling pipes were attached to the printed burner cooling tubes using a compression fitting, and the inlet water cooling line is controlled to 16 °C. The mass flow rate of water into the burner is controlled using a rotameter and set to approximately 1.1 L/min. It was observed that due to the relatively low pore sizes and bulk density, the cooling water temperature responded relatively quickly to changes in the flames established over the burner. Temperatures measurements of the inlet and outflow flows were not explicitly taken during each flame, however, it was observed that temperature differences were typically below 1 °C. IR thermometer measurements over the burner surface taken at the instant the flame is turned off show the burner remains cool, and therefore, it is expected that no preheating of the fuel mixture takes place.

Both >99.9% pure methane (CH_4) and ethylene (C_2H_4) are tested
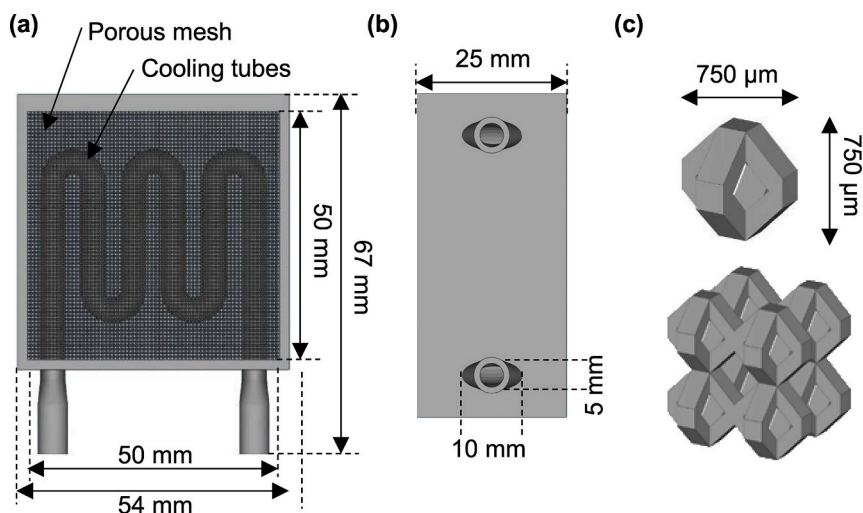

Fig. 1. CAD model of the 3D printed burner (a, b), with the unit cell utilised for the mesh (c).

individually and premixed with Halon-1301 (CF$_3$Br) and nitrogen (N$_2$) at the desired volume fraction using digital mass flowrate controllers with an absolute accuracy better than 1%. The selection of the fuels is intended to study the limit states of vertical boundary layer stabilisation as methane has a particularly low laminar flame speed and C/H ratio relative to ethylene. A premixed fuel-inhibitor mixture is supplied into the gas plenum and porous stainless-steel burner to generate a boundary layer flame once the gas mixture is ignited using a pilot flame. The flow rate for both fuels is fixed and was set to 1.50 L/min, with the flow rate of CF$_3$Br gradually increased until the blow-off was obtained. The total mixture flow rate increases with inhibitor volume fraction, which also increases the bulk injection velocity.

OH-PLIF was generated by a frequency-doubled output of a 10 Hz pulsed Nd:YAG laser (Spectra Physics Pro-350) which pumps a Sirah dye laser using Rhodamine 6G in ethanol. The output is frequency doubled to produce an ultraviolet (UV) laser beam at 283.01 nm exciting the Q$_1$(6) bandhead of OH for excitation for the A$^2\Sigma^+$-X$^2\Pi$ (1,0) system. The UV beam is passed through two cylindrical lenses to form a vertical laser sheet of approximately 20 mm × 300 μm onto the centerline of the burner (25 mm along the burner width). The laser sheet length from the bottom of the mesh is approximately 15 mm. This laser sheet positioning is intended to focus primarily on the leading edge. A schematic of the experimental set-up is shown in Fig. 2 The energy of the laser sheet was 7 mJ/pulse, with OH-PLIF produced in the partially saturated regime. Operation in the partially saturated regime was quite advantageous as the OH signal intensity remains linearly correlated with the OH concentration and is less sensitive to variations in laser energy and quenching environment (which is strongly influenced by precursors), whilst also maximizing the SNR. The OH-PLIF signal was collected by a LaVision Imager Intense CCD camera lens coupled to an 18 mm, UV intensifier (Photonis XX1450VD), with a gate time of 200 ns. The camera and intensifier set-up are coupled to a 105 mm, f#=4.5, UV Nikkor lens and a 310 nm, 10 nm FWHM bandpass filter to completely eliminate laser reflections. The camera viewing window was 15.3 mm × 18.7 mm, with a projected pixel size of 29.5 μm/pixel, to focus on the characteristics of the leading edge of the boundary layer flame. Images were acquired at 10 Hz, and for each flame case, 1000 images were taken, which was found to be sufficient to obtain statistically converged data on the flame geometry and stability. A baseline set of images for solely CH$_4$ and

C$_2$H$_4$ were taken to provide both qualitative and quantitative comparisons to the chemically inhibited flame cases.

2.2. Data processing

The OH-PLIF images are subsequently post-processed to correct for camera background noise, intensifier flat fields, and the laser sheet profile. These form the basis for post-processing to obtain useful flame characteristics defining flame stability such as the flame stand-off distance, reaction zone width, leading edge curvature, leading edge reactivity, and the location and movement of the leading edge. Fig. 3 provides an example of the quantitative data processing methodology taken for analysing the OH-PLIF images. Corrected images are binarized using a Moore-Neighbour tracing algorithm to isolate the reaction zone. A sequence of filters is applied to remove spurious signals. The flame stand-off distance is obtained to a pixel-wide resolution (29.5 μm) by skeletonizing the peak OH region in the image. This approach offers considerably more advantages in terms of accuracy compared to traditional line-of-sight SLR imaging thresholding approaches [17].

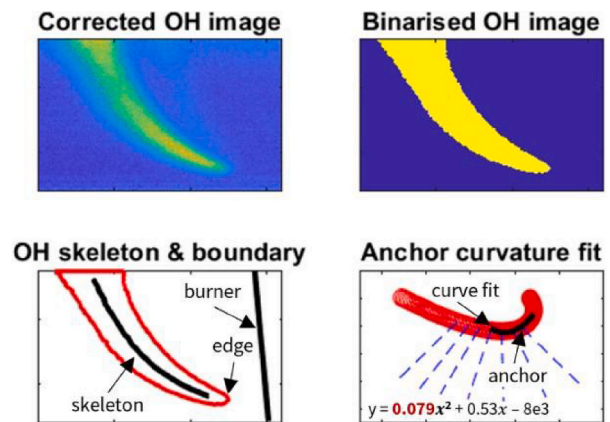The flame skeleton does not identify the exact coordinates of the

Fig. 3. Example image processing sequence from the corrected OH-PLIF image to flame anchor curve fitting.
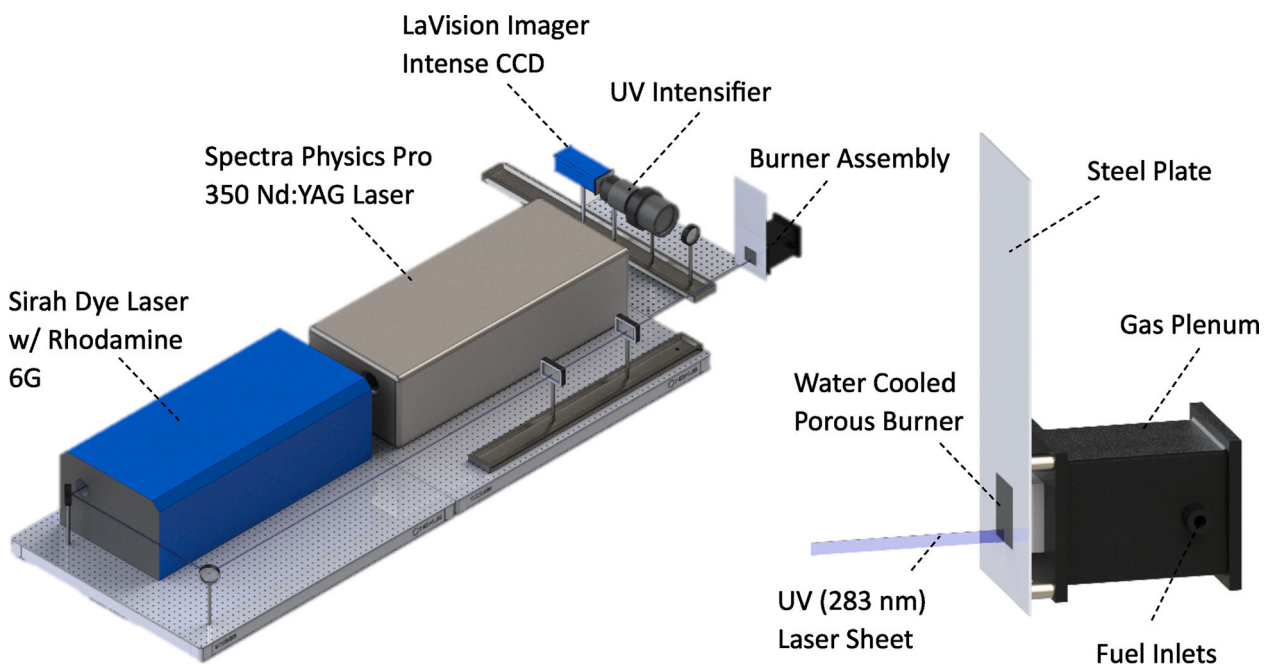

Fig. 2. Experimental setup showing the laser, burner and OH-PLIF collection optics and right the orientation of the laser sheet relative to the burner.

leading edge. An algorithm was developed to automatically identify the discrete location of the leading edge by tracing along the OH layer boundary and calculating the local curvature of the 2D line within the flame anchor area at a resolution of 5 neighbouring pixels. The region of greatest analytical curvature was defined as the leading edge. The overall leading-edge curvature is then defined by the first polynomial constant from a second-order polynomial fit to the leading edge location using 15 neighbouring pixels.

3. Results

Blow-off extinction for CH_4 is obtained at 15.7% CF_3Br volume addition (compared to 70% for N_2), while for C_2H_4, extinction occurs at 37.3% CF_3Br addition (extinction was not identified for N2 at 76%). The temporal blow-off process appears to be stochastic during the image acquisition period for both cases (100 seconds), though these concentrations represent hard stability limits. At this point, the flame partially lifts off the burner surface, or moves out of plane and stabilizes downstream of the viewing window constantly, however, only complete extinction is considered. The minimum extinguishing concentrations (MECs) observed for the vertical boundary layer diffusion flames are remarkably greater than reported values in the literature for canonical configurations such as a counterflow burner (2.5%) [18], co-annular tube jet burners (2.3–4.1%) [19,20], and buoyant cup-burners (2.4%) [21].

3.1. Flame structure

Ensemble mean OH-PLIF images (500 images) accompanied by DSLR images (6000 images) are shown for both the CH_4 (Fig. 4) and C_2H_4 (Fig. 5) flames inhibited by CF_3Br at increasing inhibitor volume fractions. The OH signal in each image is normalised by the maximum signal measured. The green boundary on the DSLR images shows the 50% flame intermittence within the ensemble of images. Both fuels show characteristic boundary layer profiles established over the fuel plate, with the flame anchored at the leading edge. The OH-PLIF images also show a canonical "edge flame" structure [8] rather than a triple or "tribrachial" flame with a lean and rich branch stabilizing the stoichiometric reaction zone kernel, which has been hypothesized in the fire

research literature for boundary layer flames established over solid fuels dating back to the seminal work of de Ris [22]. The physical structure of the leading edge for these flames has been difficult to verify due to blurring difficulties that arise in line-of-site imaging techniques such as an SLR camera. The structure of the leading edge resembles numerical calculations by Chen and T'ien [7].

As CF_3Br is added to the fuel stream, the overall flame length initially starts to increase considerably. As the blow-off limit is approached, the flame length subsequently starts shortening, however, in the case of C_2H_4, the anchored leading edge continues to be sustained. The shortening of the flame length can be viewed in the C_2H_4 OH-PLIF image window in Fig. 5, however, for CH_4, extinction occurs while the flame is still entirely within the image window, indicating inherently different chemical responses at both the leading and trailing edges towards blow-off. DSLR images also reveal dramatic increases in soot emission. CH_4 flames shift from a dark blue colour dominated by CH* and C_2 emission to yellow as X_{inh} is increased which is consistent with observations of inhibited laminar flames [20]. Comparatively, the C_2H_4 flames show a remarkable change in sooting characteristics with inhibitor addition with the flame shifting from bright blue/yellow to a dark orange flame that smokes considerably, highlighting that the flame tip has completely opened.

The chemical structure of the CH_4 and C_2H_4 flames revealed by OH-PLIF are shown to be different. For CH_4, the reaction zone broadens, along with the region of peak OH fluorescence shifting further downstream with inhibitor addition towards $X_{inh} = 0.153$. In contrast, the C_2H_4 flames maintain their characteristic boundary layer structure until $X_{inh} = 0.165$, at which the OH reaction zone starts to shorten dramatically towards $X_{inh} = 0.373$. Simultaneously, a secondary fluorescence branch on the rich side of the diffusion flame is detected. Both the size and intensity of this branch increase with CF_3Br volume fraction addition. It is worth noting that this branch was also detected for both CH_4 and C_2H_4 flames, however, the signal of this branch closely approximates the camera background and is therefore eliminated during image filtering. This branch is not observed for the flames pre-mixed with N_2. The presence of this branch is likely related to the broadband fluorescence of soot precursors and will be discussed later.

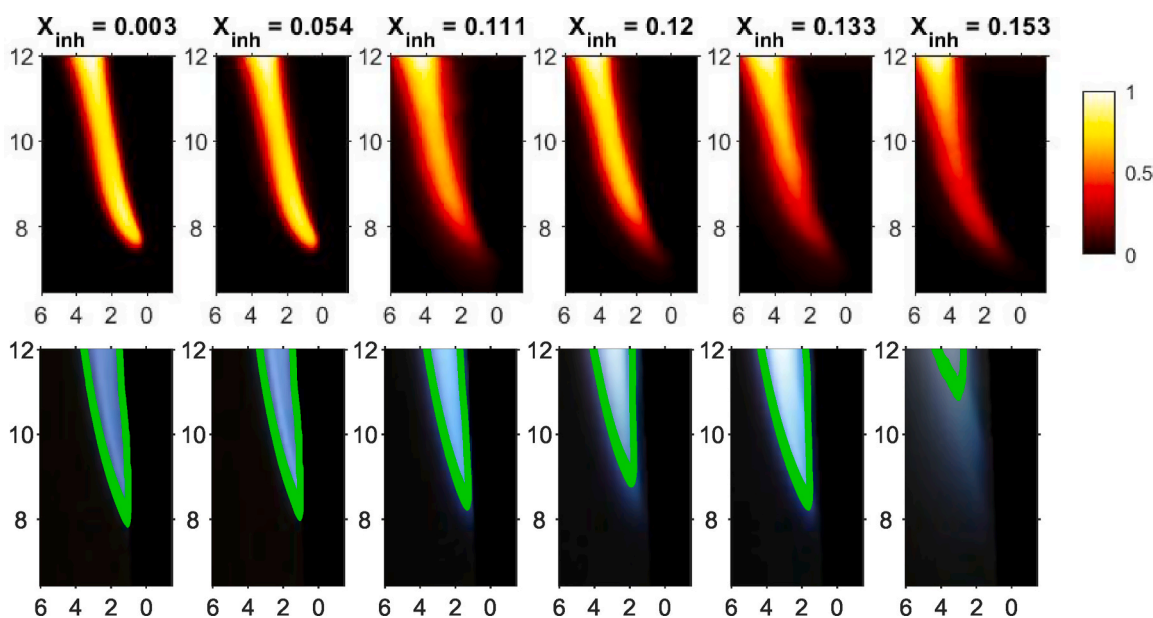Fig. 6(a and b) shows the axial distribution of the mean flame stand-off distance and OH layer thickness for the CH_4 and C_2H_4 flames

Fig. 4. Ensemble mean normalised OH-PLIF and DSLR images of CH_4-CF_3Br premixed mixtures at a few selected inhibitor volume fractions. The green boundaries in the DSLR images represent the 50th percentage flame intermittency. (For interpretation of the references to colour in this figure legend, the reader is referred to the Web version of this article.)

Fig. 5. Ensemble mean normalised OH-PLIF and DSLR images of C_2H_4-CF_3Br premixed mixtures at a few selected inhibitor volume fractions. The green boundaries in the DSLR images represent the 50th percentage flame intermittency. (For interpretation of the references to colour in this figure legend, the reader is referred to the Web version of this article.)
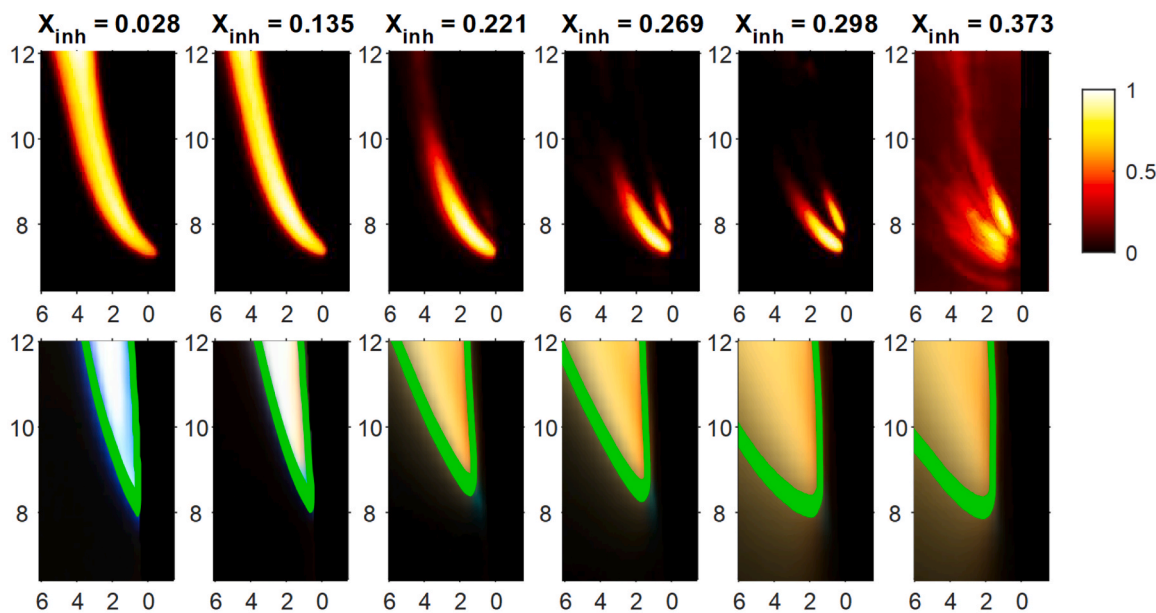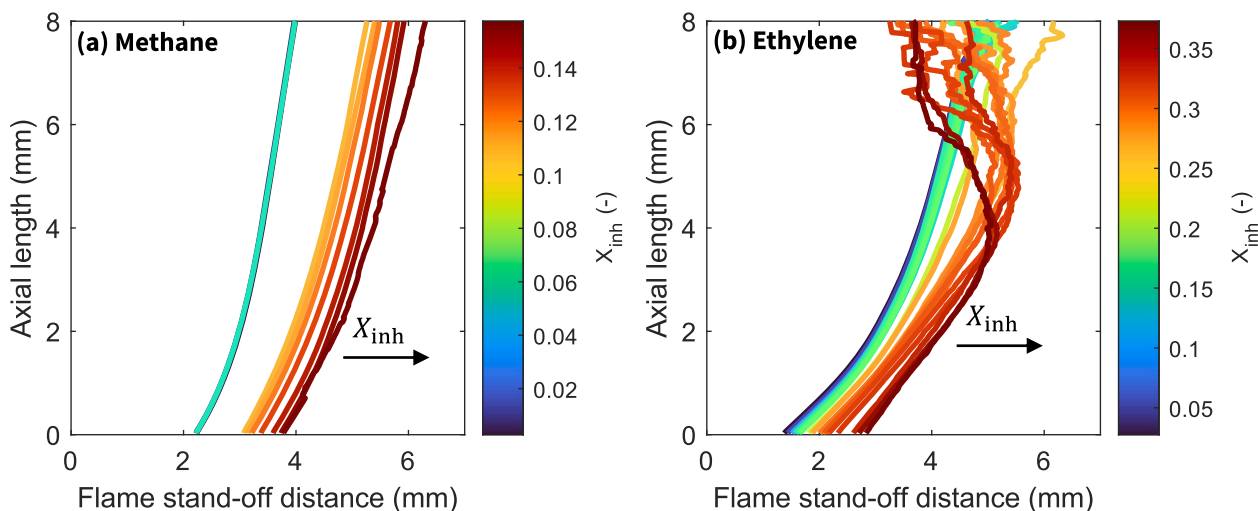

Fig. 6. Mean flame stand-off distance for (a) CH_4 and (b) C_2H_4 flames inhibited by CF_3Br.

inhibited with CF_3Br at increasing volume fractions. In the case of all the CH_4 flames and the C_2H_4 flames at low values of X_{inh}, a characteristic laminar boundary layer profile is maintained; however, the trend shows a distinct positive correlation between the flame stand-off distance and X_{inh}. Dramatic increases in the flame stand-off distance are only observed as X_{inh} is increased substantially ($X_{inh} = 0.11$ for CH_4 and 0.20 for C_2H_4). The non-linear increase in the flame stand-off distance with X_{inh} suggests that the alterations in the flame chemistry due to the brominated and fluorinated species are responsible for the flame structure changes rather than an increased bulk flow velocity. As X_{inh} is increased beyond 0.20 for C_2H_4, the mean stand-off distance continually decreases with the axial distance and strong fluctuations are observed approximately 4 mm from the leading edge, indicating that the boundary layer has separated resulting in a shorter anchored OH reaction zone layer.

Axial distributions of the mean OH layer thickness are shown for the CH_4 and C_2H_4 flames in Fig. 7(a and b) respectively. The OH layer thickness for C_2H_4 possesses different profiles to the CH_4 flames, which asymptote at approximately 4 mm downstream from the leading edge. In the case of C_2H_4, the OH layer thickness starts extremely narrow (<0.4 mm), suggesting a "narrow" flame anchor point. This is expected given the very large laminar flame speed and reactivity of ethylene. As X_{inh} increases, the reaction zone for CH_4 near the leading edge broadens and effectively stabilises before the attainment of blow-off. Towards the trailing edge, this trend somewhat reverses, and the thickness reduces slightly. The broadening of the reaction zone suggests that the kinetics at both the leading edge and downstream slow due to CF_3Br presence, however, this effect dampens until blow-off is attained.

Ethylene flames exhibit a completely different trend, with the OH layer thickness decreasing non-linearly with X_{inh}. Moreover, the primary OH layer shortens, with separation of the boundary layer observed by fluctuations in the mean thickness occurring downstream. Flow separation occurs earlier along the streamwise direction than the CH_4 flames due to the larger heat release rate and consequently buoyancyper unit
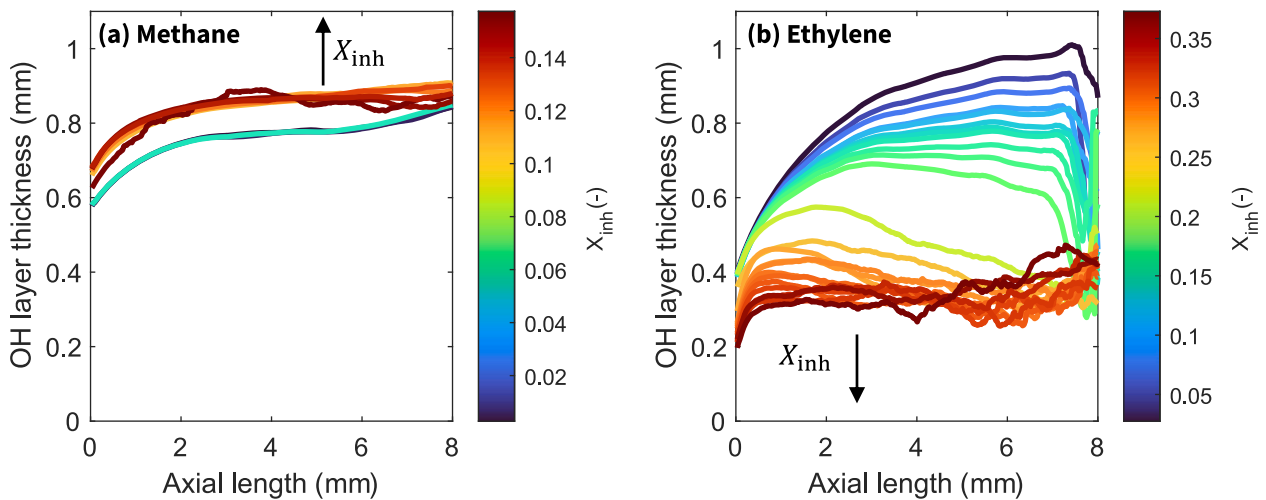
Fig. 7. Mean OH reaction layer thickness for (a) CH_4 and (b) C_2H_4 flames inhibited by CF_3Br.

volume. The addition of CF_3Br reduces the laminar flame length, however, the flame is still able to be sustained at small OH layer thicknesses relative to the CH_4 flames despite the very large inhibitor volume fractions.

3.2. Leading edge stability

The stabilisation of the leading edge is analysed by quantifying and subtracting the instantaneous axial (y-component) and normal (x-component) position for the flame anchor from the mean anchor point coordinates at $X_{inh} = 0$. Mean and rms displacements for the CH_4 and C_2H_4 flames at various values of X_{inh} are shown in Fig. 8(a and b). The results show that both the mean normal and axial displacements for the flame anchor increase once enough inhibitor is added to the fuel stream. The divergence of the mean and rms values indicates a destabilised fluctuating flame anchor and is shown to occur only in the axial direction at larger inhibitor concentrations. Upon contrasting both flames, it is remarkable to observe the relative stability of the C_2H_4 flame anchor relative to CH_4 along the axial direction. Axial fluctuations only occur after $X_{inh} = 0.33$, however, the mean position appears highly insensitive to CF_3Br addition compared to the CH_4 flames, which restabilises downstream approximately 2 mm before blow-off. It is also worth noting

that the anchor displacement normal to the wall does not follow a linear trend with X_{inh} suggesting that a slower reaction speed, rather than the increased bulk flow injection velocity in the fuel stream controls the flame anchor position. Similar displacements are obtained in cup-burner flames featuring methane and propane inhibited by CF_3Br, however, these occur at smaller volume fractions [23,24], indicating that the leading edge reactivity and Damköhler number is sufficiently large enough for the flame to continually re-anchor downstream axially along the vertical porous fuel plate.

Fig. 9(a and b) shows the fitted curvature of the flame anchor as a function of X_{inh}. Larger values of curvature correspond to a broader anchor (i.e. the parabola from the vortex widens). Both fuels possess distinct baseline anchor curvatures, likely associated with the different laminar flame speeds. As X_{inh} is added, the flame anchor continually broadens for CH_4 and is consistent with the slowing of the kinetics due to radical scavenging effects. Interestingly, a different trend is observed for C_2H_4, where the anchor curvature increases, which shows that the flame anchor is effectively "squeezing", with significant fluctuations observed once $X_{inh} > 0.30$.
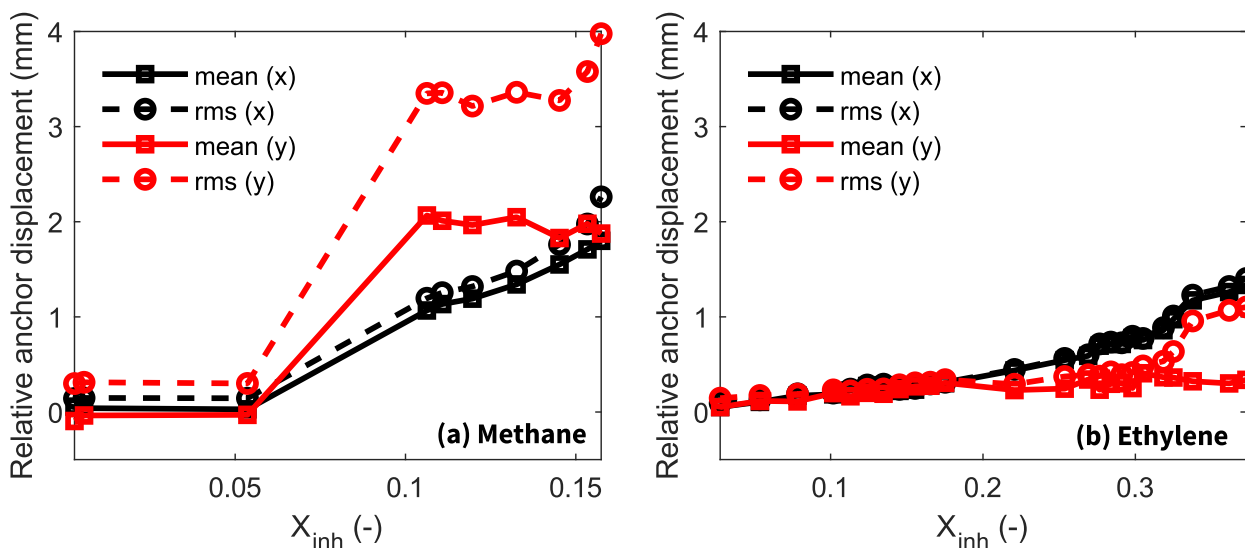

Fig. 8. Flame anchor point displacement relative to the uninhibited case for CH_4 (a), and C_2H_4 flames (b) as a function of inhibitor volume fraction. The x-component corresponds to displacement normal to the wall, and the y-component corresponds to axial displacement.
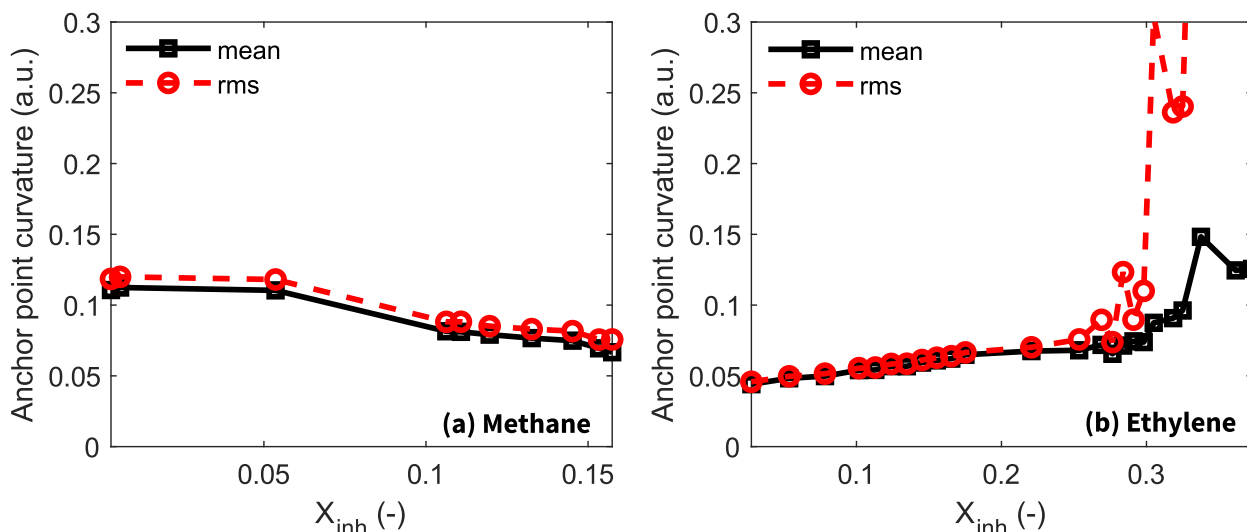
Fig. 9. Flame anchor point curvature for CH_4 (a), and C_2H_4 flames (b) as a function of inhibitor.

3.3. Flame chemistry

3.3.1. Chemical equilibrium and laminar flame speed calculations

The preceding analysis shows remarkable differences in the chemical effects of CF_3Br on the stability of the leading edge for the CH_4 and C_2H_4 flames. To help infer chemical effects from the fluorescence data, chemical equilibrium computations have been performed using Gaseq, along with 1-D laminar flame speed calculations using the freely propagating flame model in Cantera. Computations have been performed considering the presence of fluorinated and brominated product species. The chemical mechanism implemented by Pagliaro et al. [25] based on the CF_3Br model by Babushok et al. [26] for $C_1 - C_4$ fuels are used for the laminar flame speed calculations.

Fig. 10(a) shows the variation of the stoichiometric mixture fraction (f_{st}) for CH_4 and C_2H_4 premixed with CF_3Br, with N_2 also shown as reference. The calculation of f_{st} is strongly driven by both the carbon and fluorine atoms in CF_3Br, which appears in the post-combustion products as HF and CO_2/CO. Brominated species do not significantly influence f_{st} as Br_2, HBr, Br are key catalytic recombination species in the scavenging process that drive radicals towards equilibrium [19]. The results show a strong influence of CF_3Br on f_{st}, which increases significantly with X_{inh} compared to N_2. This increase implies lower A/F (air to fuel)

requirements for burning, meaning that the flame sheet should be rich shifted with X_{inh}. This is counterintuitive as the experimental results show the reaction zone broadening and shifting further away from the fuel surface. This suggests that CF_3Br is preferentially decomposing on the rich (fuel stream) side and reacting with both O_2 and intermediate fuel molecules on the rich side of the diffusion flame. Therefore, any leftover fuel intermediates effectively leak through the reaction zone resulting in a broader and longer flame as species are advected by the buoyancy-induced flow field. The adiabatic flame temperature (black lines), shown in Fig. 10(b), is observed to be somewhat insensitive to X_{inh} within the blow-off limits of the experiments with temperature changes between 50 and 100 K. Changes in the OH mole fraction in the post-combustion products are considerably more sensitive. This is a useful result as the experimental OH fluorescence signal is a marker for the OH mole fraction due to the temperature insensitivity resulting from operating in the partially saturated regime.

Normalised laminar flame speed ($\overline{S_L}$) results from the kinetic model for both CH_4 and C_2H_4 flames inhibited by CF_3Br at increasing X_{inh} at $\varphi = 1$ is shown in Fig. 11. While the model formulation is not relevant to the experimental configuration, the laminar flame speed is a useful surrogate for flame reactivity to assess the sensitivity of both the reaction pathways for CH_4 and C_2H_4 to CF_3Br. Smaller inhibitor volume
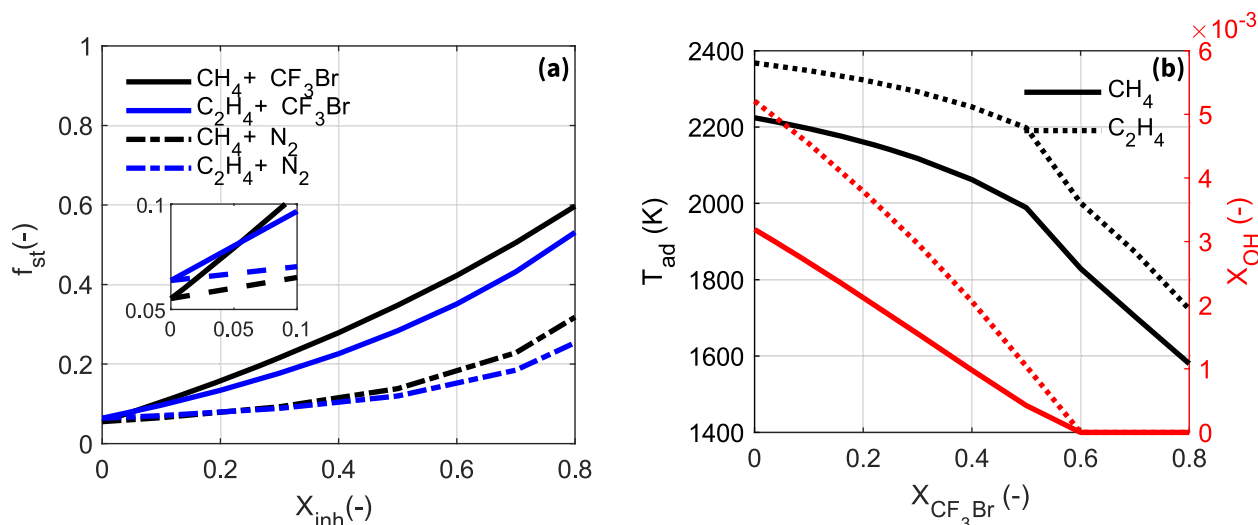

Fig. 10. Stoichiometric mixture fraction (a) and Adiabatic flame temperature (b) for the N_2 diluted and CF_3Br inhibited CH_4 and C_2H_4 flames.
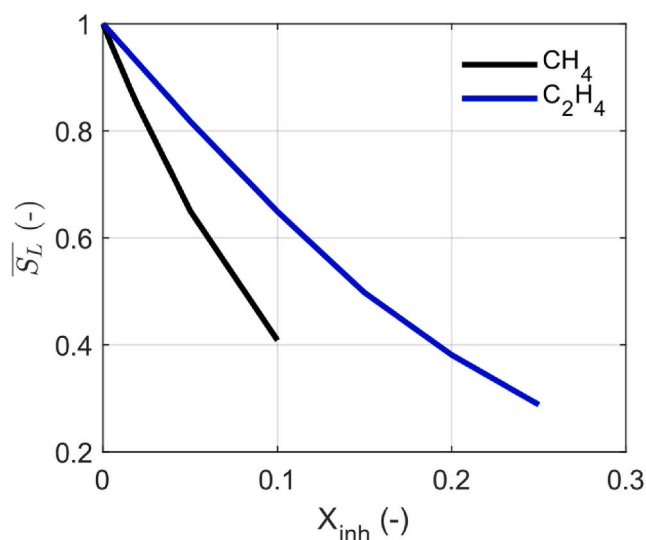
Fig. 11. Normalised laminar flame speed calculations of CH_4 and C_2H_4 inhibited by CF_3Br as a function of X_{inh}.

fractions relative to the experiments are modelled due to numerical stability issues, however, these results are intended to be phenomenological. The results show that CH_4 is considerably more sensitive to CF_3Br compared to C_2H_4, with considerably larger values of X_{inh} needed to produce the same reduction of $\overline{S_L}$. The computations align with the experimental measurements of flame stability and structure shown earlier at the leading edge, which carries high reactivity with the largest radical pool concentrations [27].

3.3.2. Leading edge radical pools

The mean OH intensity at the leading edge has been obtained by dividing the integrated fluorescence signal by the fluorescing area within a 50 pixel (~1.5 mm) window from the axial flame anchor coordinate upwards. This window is traced along the OH layer boundary (Fig. 3). Recalling from the equilibrium calculations earlier that the OH fluorescence intensity effectively is a measure of the OH radical pool concentration. OH intensities at the leading edge for both fuels are shown in Fig. 12(a and b). For the CH_4 flames, the OH concentration at the leading edge increases with X_{inh} prior to plateauing at $X_{inh} = 0.119$ and dropping dramatically before the blow-off limit. Comparatively, for C_2H_4, there is little response to the OH concentration until $X_{inh} = 0.175$,

at which point the radical pool starts to steadily decrease at a slow rate until blow-off is attained. The increase in the OH concentration for CH_4 and the initial insensitivity for C_2H_4 suggests that oxygen entrainment into the flame anchor is enhanced due to the increased trailing edge flame length, which imposes a greater buoyancy-induced velocity. This will be discussed in more detail shortly.

3.3.3. Broadband precursor fluorescence

Detection of an additional fluorescence branch formed on the rich side of the diffusion flame was observed for both CH_4 and C_2H_4 flames inhibited with CF_3Br. The intensity of this fluorescence branch was considerably more pronounced for ethylene at larger inhibitor volume fractions and did not appear when the fuel was premixed with N_2, suggesting some unique chemical interaction with the brominated or fluorinated species. Fig. 13 shows the ensemble mean (100 images) of a fluorescence signal for a C_2H_4 flame inhibited by CF_3Br at $X_{inh} = 0.295$ at the $Q_1(6)$ excitation wavelength for OH at 283.01 nm, and a slightly detuned wavelength at 283.0081 nm. The off-wavelength scan reveals that the inner branch on the rich side of the flame sheet remains possesses broadband molecular fluorescence emission characteristics. Similar observations have been made by Smyth et al. [20] and are attributed to soot precursors, which track well with increases in flame luminosity and soot/smoke production revealed by the DSLR images (Fig. 5). The opening of the flame and observed "smoking" at the trailing edge for large values of X_{inh} is likely why the trailing edge length decreases significantly.

The broadband fluorescence branch size and intensity increase with the addition of CF_3Br, suggesting that the decomposition reactions for the inhibitor take preference on the rich side. These results are consistent with Raman measurements of $CFBr_3$, HF, and HBr by Masri et al. [28] in CH_4-CF_3Br flames, which show large mass fractions at large mixture fractions relative to the peak OH concentration and stoichiometric mixture fraction. The prevalence of HF and HBr molecules in those measurements on the rich side shows that decomposed H from the fuel is consumed by the inhibitor intermediates, thereby increasing the local C/H ratio, resulting in enhanced precursor and soot formation. Greater soot formation towards the trailing edge enhances radiative losses resulting in radiative quenching at the flame tip.

4. Discussion

The analysis presented hitherto demonstrates that the inhibitor certainly influences both the leading-edge stability and the trailing-edge length. Nevertheless, the effects of the brominated and fluorinated
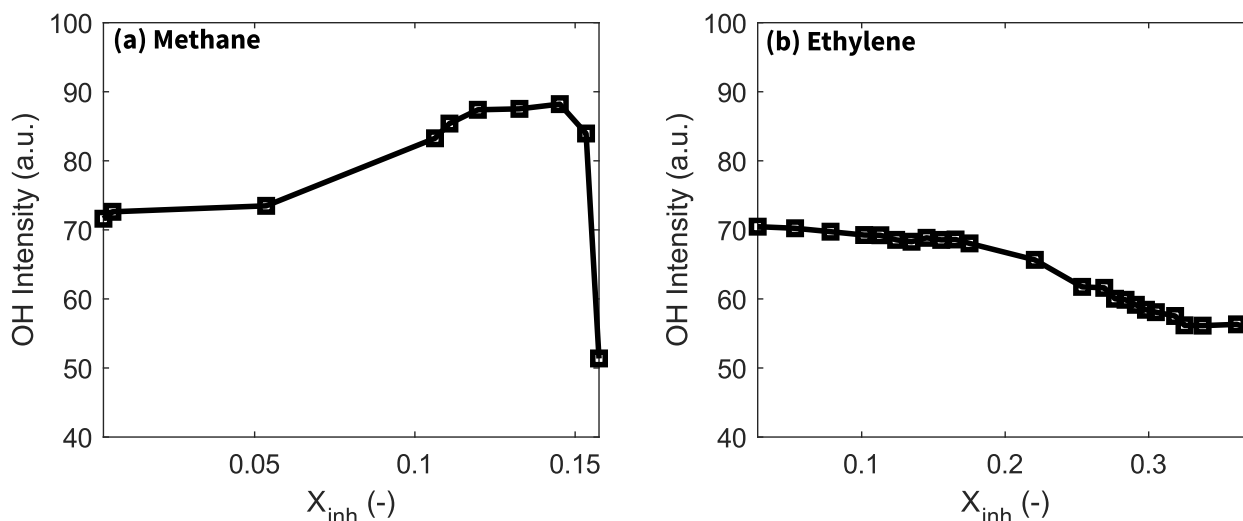

Fig. 12. OH peak intensity in the flame stabilization region for CH_4 (a), and C_2H_4 flames (b) as a function of inhibitor.
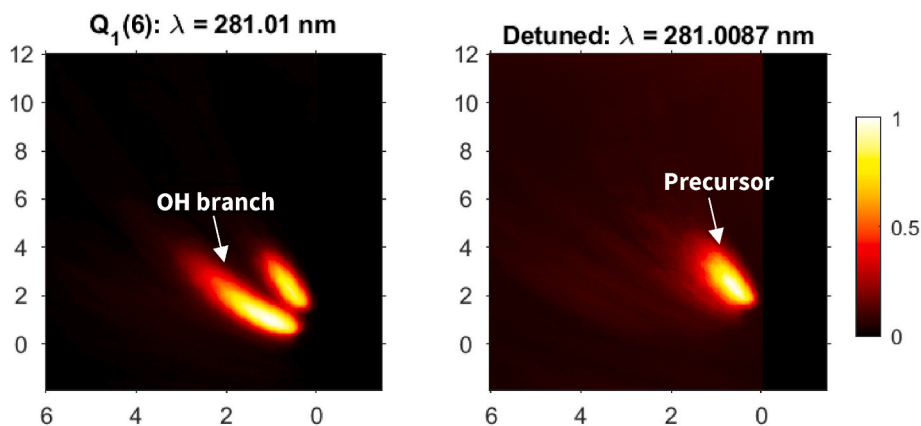
Fig. 13. Mean PLIF images for the C_2H_4 flame case on the OH $Q_1(6)$ transition wavelength (left) and off-wavelength (right) confirming the spatial assignment of OH and precursor fluorescence regions.

species in the inhibitor on the chemical timescale and reactivity on the leading edge are certainly dampened by the presence of a vertical porous fuel plate, which alters the flow residence time while providing the conditions for the leading edge to continually re-anchor downstream axially. This is a unique characteristic compared to other natural convective configurations such as a cup burner and forced counterparts (counter flow burner) where the oxidiser strain rate is explicitly controlled. Stability at the flame leading edge is controlled by the local Damköhler number [9]:

$$Da = \frac{\tau_{res}}{\tau_{chem}} = \frac{\rho_\infty k_{eff}}{\left(U_\infty^2 / \alpha_\infty\right)} \qquad (1)$$

where ρ_∞ is the free stream density, U_∞^2 is the buoyancy-induced velocity, α_∞ is the thermal diffusivity of the free stream, and the effective rate constant is represented by an Arrhenius expression $k_{eff} = A_0 T_F \exp(- E / R T_F)$. The experimental and numerical results clearly show that CF_3Br slows the reaction rate. At the leading edge, U_∞ is the local free-stream velocity that is being heated to the partially premixed flame temperature at the reaction kernel over one thermal length, δ_L. In the formulation by Chen and T'ien, the thermal length and local velocity are defined by the thermal diffusivity near the leading edge [7]. However, numerical simulations of vertically spreading flames by Johnston et al. [11] have revealed that buoyancy-induced forces accelerate the flow ahead of the leading edge by upwards of 30% for a 60 cm long flame. These are similar flame lengths to the flames studied in this paper. The upstream acceleration of the flow by the flame length imposes strain at the leading edge. Measuring the local velocity at the leading edge is difficult, however, this value is bounded by a characteristic leading-edge buoyancy-induced velocity, which can be written as:

$$U_\infty = (\beta g L_F \Delta T_F)^{1/2} \qquad (2)$$

where L_F is the trailing edge length, and ΔT_F is the temperature rise from the free stream to the leading edge. The equilibrium analyses conducted earlier show that CF_3Br effects on ΔT_F at the leading edge are mild [24], and therefore the residence time is effectively controlled by L_F. The dampening effect on the reactivity arises because O_2 transport into the leading edge is enhanced due to an increased mass flux. Diffusion of H from the leading edge into the oncoming O_2-rich flow enables the chain branching reaction [21,29]:

$$H + O_2 \rightarrow OH + O \qquad (3)$$

This reaction effectively dampens the scavenging effect of the brominated species by replenishing the OH radical pool, thereby promoting reactivity and increasing stability as $Da \propto X_{OH}$ [30]. Similar phenomena have been observed under forced flow conditions [31]. Leading edge de-stabilisation is observed to occur once the trailing edge

length decreases as X_{inh} increases likely due to a combination of the greater radical concentrations at the trailing edge [21], resulting in a more efficient catalytic cycle, and radiative quenching effects that result from the opening of the flame tip. As the flame length decreases, O_2 transport into the reaction kernel reduces. Considering the larger scavenging radical concentrations at the leading edge at the large limit of X_{inh}, the Damköhler number reduces triggering de-stabilisation and blow-off from the leading edge. The comparatively larger laminar flame speed and radical pool for the C_2H_4 flames are likely why the flame length can be reduced significantly while remaining anchored at large CF_3Br concentrations.

This is a rather unique trailing edge length-controlled mechanism for blow-off compared to the other flames. Leading edge stability is both controlled by the flame anchor reactivity and the trailing edge length, which defines the residence time. Both parameters are inherently coupled to the fuel/inhibitor flame speed and X_{inh}. However, the results show that due to this coupling that is driven by strong buoyancy-induced flows, considerable volume fraction addition of inhibitors is required to bring vertical boundary layer flames to the blow-off limit. Inert agents relying on thermal dilution are likely to be more difficult to attain blow-off. These results have direct relevance to vertical wall fires found in compartment fires and external building facades. Both chemically active and inert fire-retardants embedded in combustible composite materials are likely to be ineffective at inducing blow-off within the gas phase. Instead, these materials contribute towards extinction by reducing the overall burning rate of the solid and by acting as an additional heat sink in the solid phase.

5. Conclusions

The leading-edge stabilisation mechanism for buoyancy-driven vertical boundary layer diffusion flames has been experimentally studied using a novel 3D-printed porous burner. The stability of both methane (CH_4) and ethylene (C_2H_4) flames were modified by adding increasing volume fractions of Halon-1301 (CF_3Br) to the fuel stream. Extinction driven by blow-off was attained for CH_4 at $X_{inh} = 0.157$ and for C_2H_4 at $X_{inh} = 0.373$, which are remarkably larger extinction concentrations compared to other canonical configurations. The structure and stability of the leading-edge stability are studied through measurements of OH-PLIF. The results show that the flame length increases with X_{inh} due to the slowing of the kinetics, however, as the blow-off limit is approached, the flame length subsequently decreases followed by the destabilisation of the flame anchor. Significant reductions in the flame length for ethylene are observed, along with promoted soot formation and eventual opening of the flame tip followed by smoking. Despite this, the flame anchor is remarkably stable until the blow-off limit is attained. The reaction zone for methane broadens, however, the opposite is found for ethylene

indicating distinctly different chemical kinetic pathways, with ethylene being considerably less sensitive to inhibitor addition. This experimental observation is verified through laminar flame speed calculations at a unity equivalence ratio. Calculations of the stoichiometric mixture fraction (f_{st}) for both fuels show significant non-linear increases as CF_3Br is added into the reactant stream, implying rich shifting of the flame sheet. This contradicts measurements of the flame stand-off distance, which increase with X_{inh}. It is believed that the decomposition and oxidation reactions of CF_3Br occur preferentially on the rich side, with fuel leaking through the reaction zone, resulting in the broadening observed experimentally. This appears to be confirmed by the presence of broadband molecular fluorescence on the rich side of the flame sheet. This is attributed to soot precursors that are driven by the presence of high concentrations of brominated intermediate species that also track with the increased luminosity and sooting from the flame. The broadband fluorescence signal is shown to increase with X_{inh} for ethylene flames.

Measurements of the OH fluorescence intensity at the flame anchor for both fuels show that OH concentrations either increase (CH_4) or remain constant (C_2H_4) as CF_3Br is initially added. There is also a corresponding increase in the flame length at the trailing edge due to additional heat release from the inhibitor species and reduced kinetics. Once the flame length reduces towards larger CF_3Br concentrations, the OH radical pool at the leading edge depletes, albeit at different rates due to the distinct differences in the flame speed and chemical pathways of methane and ethylene. Based on these findings, the large blow-off limits relative to other flame configurations with controlled strain rates such as cup or counterflow burners are associated with a dependency on the buoyancy-induced velocity on the trailing edge flame length. Longer flames enhance O_2 transport into the flame anchor, which replenishes the OH radical pool and dampens the effect of the inhibitor on the stability of the flame anchor, which stabilizes to the fuel plate slightly downstream as X_{inh} increases. It is only when the flame length decreases due to efficient catalytic recombination at the trailing edge that the reduction in O_2 transport combined with reduced kinetics at the flame anchor results in blow-off extinction.

The unique extinction mechanism identified in this work highlights the difficulty of attaining blow-off using chemically active or inert agents embedded in combustible solid fuels in realistic vertical wall fire configurations such as compartment fires or external combustible façade systems. Future work will utilize newly fabricated 3D-printed bronze burners with a larger geometry (78 × 74 x 25) and increased pore sizes that resolves the inhomogeneous flow regions observed in the prototype burner.

Declaration of competing interest

The authors declare the following financial interests/personal relationships which may be considered as potential competing interests:

Assaad R. Masri reports financial support was provided by Australian Research Council.

Data availability

Data will be made available on request.

Acknowledgements

References

[1] A.C. Fernandez-Pello, T. Hirano, Controlling mechanisms of flame spread, Combust. Sci. Technol. 32 (1983) 1–31.

[2] H.W. Emmons, The film combustion of liquid fuel, ZAMM - J. Appl. Math. Mech./Z. Angew. Math. Mech. 36 (1956) 60–71.

[3] J.S. Kim, J. de Ris, F. William Kroesser, Laminar free-convective burning of fuel surfaces, Symp. Combust. 13 (1971) 949–961.

[4] A. Ramachandra, B.N. Raghunandan, Investigations on the stability and extinction of a laminar diffusion flame over a porous flat plate, Combust. Sci. Technol. 36 (1984) 109–121.

[5] J.L. Torero, L. Bonneau, J.M. Most, P. Joulain, The effect of gravity on a laminar diffusion flame established over a horizontal flat plate, Symp. Combust. 25 (1994) 1701–1709.

[6] T. Vietoris, P. Joulain, J.L. Torero, Experimental characterization of a laminar diffusion flame in micro- gravity, J. Chim. Phys. Phys. Chim. Biol. 96 (1999) 1022–1030.

[7] C.H. Chen, J.S. T'ien, Diffusion flame stabilization at the leading edge of a fuel plate, Combust. Sci. Technol. 50 (1986) 283–306.

[8] J. Buckmaster, Edge-flames, Prog. Energy Combust. Sci. 28 (2002) 435–475.

[9] J.L. Torero, T. Vietoris, G. Legros, P. Joulain, Estimation of a total mass transfer number from the standoff distance of a spreading flame, Combust. Sci. Technol. 174 (2002) 187–203.

[10] F. Tamanini, A numerical model for the prediction of radiation-controlled turbulent wall fires, Symp. Combust. 17 (1979) 1075–1085.

[11] M.C. Johnston, J.S. T'ien, D.E. Muff, X. Zhao, S.L. Olson, P.V. Ferkul, Self induced buoyant blow off in upward flame spread on thin solid fuels, Fire Saf. J. 71 (2015) 279–286.

[12] T. Noto, V. Babushok, A. Hamins, W. Tsang, Inhibition effectiveness of halogenated compounds, Combust. Flame 112 (1998) 147–160.

[13] J.A. Senecal, Flame extinguishing in the cup-burner by inert gases, Fire Saf. J. 40 (2005) 579–591.

[14] C.K. Westbrook, Numerical modeling of flame inhibition by CF3Br, Combust. Sci. Technol. 34 (1983) 201–225.

[15] J. de Ris, L. Orloff, The role of buoyancy direction and radiation in turbulent diffusion flames on surfaces, Symp. Combust. 15 (1975) 175–182.

[16] A. Valencia, M. Talbaut, J. Yon, G. Godard, C. Gobin, A. Coppalle, Soot and velocity mapping and 2D soot sheet dimensions in a buoyant wall-fire, Proc. Combust. Inst. 36 (2017) 3219–3226.

[17] A.S. Rangwala, S.G. Buckley, J.L. Torero, Upward flame spread on a vertically oriented fuel surface: the effect of finite width, Proc. Combust. Inst. 31 (2007) 2607–2615.

[18] P. Papas, J.W. Fleming, R.S. Sheinson, Extinction of non-premixed methane-and propane-air counterflow flames inhibited with CF4, CF3H and CF3Br, Symp. Combust. 26 (1996) 1405–1411.

[19] A.R. Masri, Chemical inhibition of nonpremixed flames of hydrocarbon fuels with CF3Br, Combust. Sci. Technol. 96 (1994) 189–212.

[20] K.C. Smyth, D.A. Everest, The effect of CF3I compared to CF3Br on OH• and soot concentrations in co-flowing propane/air diffusion flames, Proc. Combust. Inst. 26 (1996) 1385–1393.

[21] G.T. Linteris, F. Takahashi, V.R. Katta, Cup-burner flame extinguishment by CF3Br and Br2, Combust. Flame 149 (2007) 91–103.

[22] J. de Ris, Spread of a laminar diffusion flame, Symp. Combust. 12 (1969) 241–252.

[23] F. Takahashi, V.R. Katta, G.T. Linteris, O.C. Meier, Cup-burner flame structure and extinguishment by CF3Br and C2HF5 in microgravity, Proc. Combust. Inst. 34 (2013) 2707–2717.

[24] F. Takahashi, V.R. Katta, G.T. Linteris, V.I. Babushok, A computational study of extinguishment and enhancement of propane cup-burner flames by halon and alternative agents, Fire Saf. J. 91 (2017) 688–694.

[25] J.L. Pagliaro, N. Bouvet, G.T. Linteris, Premixed flame inhibition by CF3Br and C3H2F3Br (2-BTP), Combust. Flame 169 (2016) 272–286.

[26] V. Babushok, T. Noto, D.R.F. Burgess, A. Hamins, W. Tsang, Influence of CF3I, CF3Br, and CF3H on the high-temperature combustion of methane, Combust. Flame 107 (1996) 351–367.

[27] F. Takahashi, W.J. Schmoll, V.R. Katta, Attachment mechanisms of diffusion flames, Symp. Combust. 27 (1998) 675–684.

[28] A.R. Masri, B.B. Dally, R.S. Barlow, C.D. Carter, The structure of laminar diffusion flames inhibited with CF3Br, Combust. Sci. Technol. 113–114 (1996) 17–34.

[29] F. Takahashi, V.R. Katta, G.T. Linteris, V.I. Babushok, Combustion inhibition and enhancement of cup-burner flames by CF3Br, C2HF5, C2HF3Cl2, and C3H2F3Br, Proc. Combust. Inst. 35 (2015) 2741–2748.

[30] H.K. Chelliah, C.K. Law, T. Ueda, M.D. Smooke, F.A. Williams, An experimental and theoretical investigation of the dilution, pressure and flow-field effects on the extinction condition of methane-air-nitrogen diffusion flames, Symp. Combust. 23 (1991) 503–511.

[31] F. Takahashi, V.R. Katta, A reaction kernel hypothesis for the stability limit of methane jet diffusion flames, Proc. Combust. Inst. 28 (2000) 2071–2078.